Re-Evaluating Water Column Reoxygenation During the End Permian Mass Extinction

F. Yang[1,2], S. Li[1], K. Y. An[3], D. P. G. Bond[4], R. Ao[1], X. B. Wu[1], L. L. Ma[1], and Y. D. Sun[1]

[1]State Key Laboratory of Biogeology and Environmental Geology, China University of Geosciences, Wuhan, China, [2]Institute of Karst Geology, Chinese Academy of Geological Sciences, Guilin, China, [3]School of Civil Engineering, The College of Post and Telecommunication of WIT, Wuhan, China, [4]School of Environmental Sciences, University of Hull, Hull, UK

Abstract Ocean anoxia is considered a key driver of the end-Permian mass extinction (EPME). However, it is much debated whether there was an ocean reoxygenation phase during, and in the aftermath, of the EPME. Evidence for ocean reoxygenation is often inferred from the absence of framboidal pyrite in some boundary marine sediments (termed the "framboid gap"). To reconstruct ocean redox evolution across the EPME, we investigated the carbon isotopic, sedimentological, and redox records of the Ruichang and Ehtan sections in South China. These documents two negative $\delta^{13}C_{carb}$ excursions and the development of anoxia associated with deepening leading up to the Permian-Triassic boundary. Above the level at which most siliceous organisms became extinct, pyrite framboid and iron proxies indicate that water column redox conditions were predominantly oxygenated but sporadically anoxic/ferruginous [non-sulfidic, free Fe(II) in the water] at Ruichang, while ferruginous conditions were more widely developed at Ehtan. These contrasting redox states are characteristic of a dynamic ocean redox landscape in the extinction interval. The "framboid gap" is seen in strata deposited under both oxic and ferruginous conditions, suggesting that the availability of decomposable organic matter for sulfate reduction additionally controlled framboid genesis. Our data confirm that oxygenated conditions were developed in some deep water basins during the EPME.

Plain Language Summary Ocean oxygen levels across the Permian-Triassic boundary, which saw Earth's greatest mass extinction (the End Permian Mass Extinction; EPME) have long been debated. Oxygen-poor (anoxic) conditions are widely implicated in the EPME. A gap in the record of pyrite framboids (small aggregates of pyrite that are commonly found in sedimentary rocks that were deposited in oxygen-poor marine environments) in some settings during the EPME is generally considered to be a function of reoxygenation at that time. We analyzed iron phase partitioning proxies (which can reveal ocean oxygen levels at the time of deposition) from two chert-bearing sections in South China. Our iron data indicate that the "framboid gap" is manifest in marine sedimentary archives that were not only well oxygenated at the time of deposition but also anoxic and ferruginous (non-sulfidic, free Fe(II) in the water). This highlights the ambiguity of the "framboid gap" in implying oxygenated conditions as well as the heterogeneous spatial nature of ocean oxygen states during the EPME.

1. Introduction

The most devastating biotic crisis in Earth's history occurred during the Permian-Triassic (P-T) transition, ca. 252 million years ago (Ma). The crisis saw the loss of over 80% of marine, and 75% of terrestrial species (Dal Corso et al., 2022; Stanley, 2016). Ocean anoxia has long been considered a key driver of the end-Permian mass extinction (EPME), supported by substantial evidence for prevailing anoxic conditions (e.g., Grasby et al., 2021; Wignall & Hallam, 1992). However, the temporal and spatial extent and intensity of marine anoxia remain debated. Some studies have identified sporadic occurrences of oxygen-rich shallow-marine refugia during the EPME and its immediate aftermath (e.g., Beatty et al., 2008; Twitchett et al., 2004). In deeper marine settings, oxygenation events have been documented based on thallium isotope records, pyrite framboid distributions, and iron phase partitioning proxies (e.g., Y. Z. Ge & Bond, 2022; Newby et al., 2021; Xiang et al., 2016).

The notion of brief episodes of reoxygenation in the P-T boundary beds finds some support in the "framboid gap"—in which pyrite framboids, a common feature of oxygen-restricted Late Permian settings—are absent in Lower Triassic strata (e.g., Chen et al., 2022). This gap, which has been identified in shallow, non-microbialite platform settings, slopes and basins, spans the marine extinction interval from *Hindeodus (H.) parvus* to lower
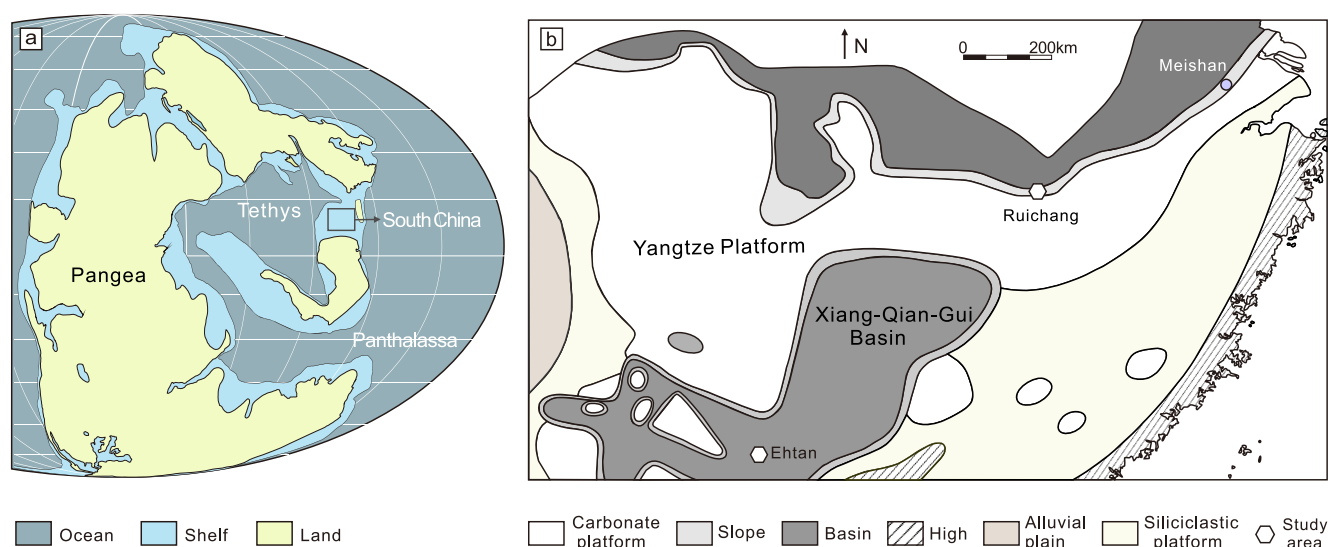
Figure 1. (a) Paleogeographic reconstruction of Pangea in the Late Permian (modified from Scotese (2014)); (b) Paleogeographic reconstruction of the South China Block during the Changhsingian (modified from Feng et al. (1996)).

Isarcicella (I.) isarcica conodont zones (e.g., Chen et al., 2022; F. Yang et al., 2022). Despite its broad recognition across the equatorial eastern Tethys, alternate redox indicators such as Ce anomalies and iron phase partitioning challenge the interpretation that the framboid gap is a definitive indicator of oxygenated conditions, with sulfate depletion potentially being responsible for the lack of framboids (e.g., S. Li et al., 2022; Müller et al., 2023). This highlights the complexity of using pyrite framboid size distributions as a redox proxy despite its increasing utility over the last two decades.

Pyrite framboids tend to form in weakly reducing conditions, particularly with elevated sulfur and iron and a low HS^-/Fe^{2+} ratio (Sweeney & Kaplan, 1973). Notably, neither greigite (Fe_3S_4), a precursor in framboid evolution, nor pyrite framboids themselves were generated in experiments where oxygen was rigorously excluded (Sweeney & Kaplan, 1973). However, pyrite framboids form in the highly restricted modern Black Sea, demonstrating their genesis in anoxic environments (Wilkin et al., 1997). The earliest Triassic framboid gap, though not yet demonstrated to be a global phenomenon, is likely a function of one of three possibilities: (a) a well-ventilated environment; (b) ferruginous conditions (anoxic, non-sulfidic condition) with limited sulfate reduction; or (c) euxinic conditions with restricted delivery of Fe^{2+}.

To probe these scenarios and decipher the intricate aspects of the framboid gap, we utilized sedimentary and geochemical proxies for redox evolution across the P-T transition in South China. The results are synthesized with prior research to document spatial and temporal variations in redox evolution and heterogeneity across the eastern Tethys.

2. Geological Setting

The South China Block (SCB) was situated in the equatorial eastern Tethys during the P-T transition (Scotese, 2014; Figure 1a). Extensive shallow-marine carbonates developed on the Yangtze Platform in the central SCB, while deeper basins were distributed along the margins of the Yangtze Platform (Feng et al., 1996; Figure 1b).

The study sections at Ruichang (Jiangxi Province; 29°41′33″N, 115°37′05″E, WGS-84) and Ehtan (Guangxi Province; 23°49′12″N, 108°58′12″E, WGS-84) record deposition in the north marginal basin of the Yangtze Platform, and the Xiang-Qian-Gui Basin. During the P-T interval, the north marginal basin of the Yangtze Platform faced Tethys, while the Xiang-Qian-Gui Basin was open to Panthalassa (Golonka, 2002).

The P-T stratigraphy at Ruichang consists of the Upper Permian Wuchiaping and Talung Formations, and the Lower Triassic Daye Formation (Figure 2a). The Wuchiaping Formation is marked by medium- to thickly-bedded (10–100 cm thick) bioclastic limestones with cherty nodules. The overlying Talung Formation consists of thinly-
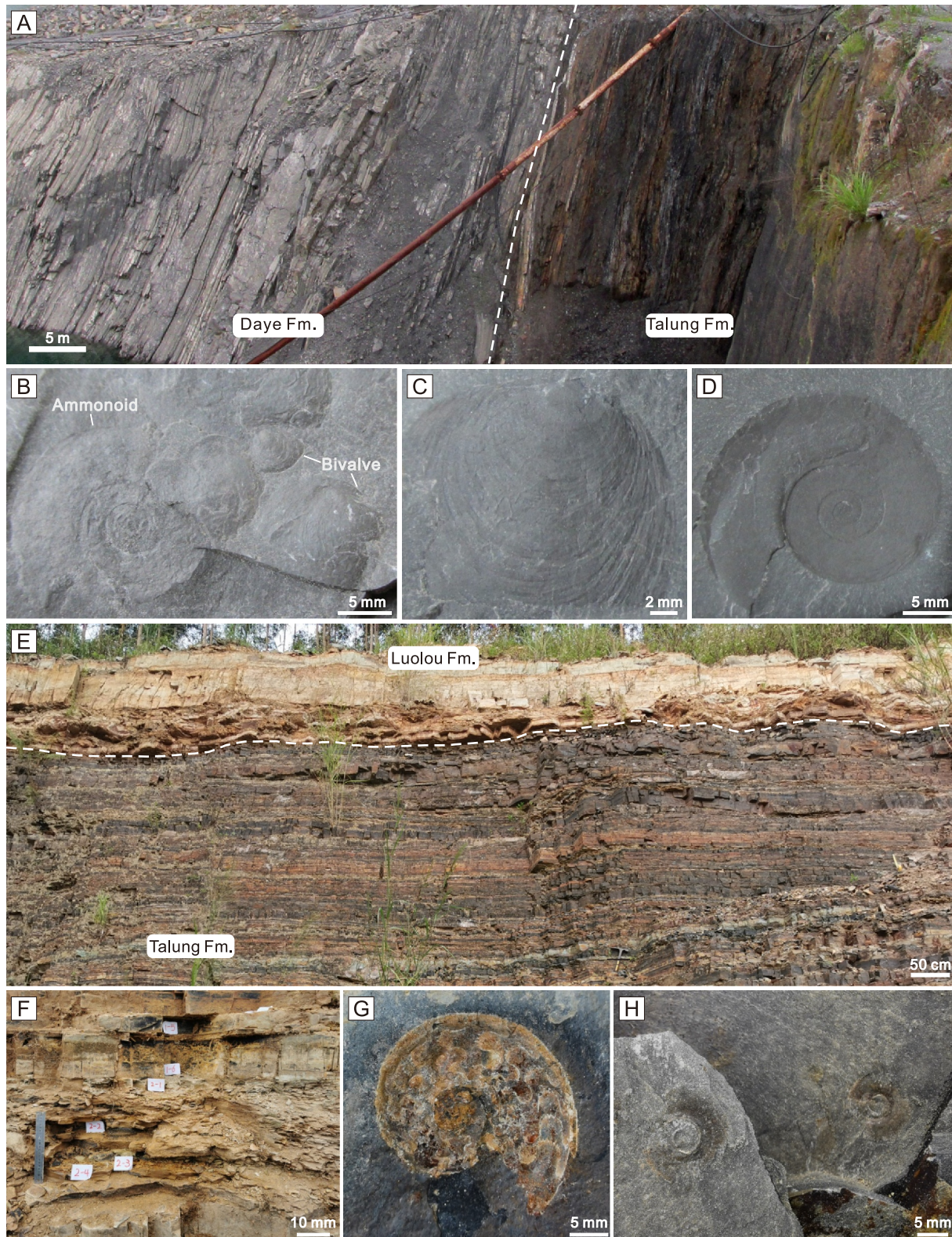
Figure 2. Field photographs showing the general characteristics of the (a–d) Ruichang and (e–h) Ehtan outcrops. (a) The main outcrop of the Ruichang section shows two lithological units. White lines represent the boundary between the Talung Formation and Daye Formation; (b) Ammonoid and bivalve imprints in the lower part of the Daye Formation; (c) *Claraia*; (d) *Ophiceras*; (e) An overview of the Talung-Luolou transition in the Ehtan section; (f) Thinly-bedded mudstones in the lower part of the Luolou Formation at Ehtan; (g and h) Ammonoid imprints in the upper part of the Talung Formation.

bedded (1–10 cm thick) spiculites and radiolarites, siliceous mudstones, cherty limestones, and shales. The Daye Formation comprises shales, mudstones, and marls. The stratigraphy at Ehtan comprises the Upper Permian Heshan and Talung Formations, and the Lower Triassic Luolou Formation (Figure 2e). The Heshan Formation is characterized by a coal-bearing limestone succession interbedded with mudstones and cherts. The overlying Talung Formation mainly comprises thinly-bedded cherts intercalated with volcaniclastic turbidites. The Luolou Formation comprises limestones, mudstones, and shales.

3. Methods

The study sections were logged in detail in the field. At Ruichang, 82 samples were analyzed for $\delta^{13}C_{carb}$, 56 of which were prepared as thin sections, 24 for pyrite framboid analysis, and 7 for iron phase partitioning characterization. At Ehtan, 50 samples were analyzed for $\delta^{13}C_{carb}$, 125 were prepared for lithological and microfacies analysis in thin section, 27 for pyrite framboid analysis, and 22 for iron characterization.

For $\delta^{13}C_{carb}$ analysis, carbonate powders (<200 mesh) were primarily obtained from micrite using a micro-drill on fresh rock surfaces. The powders reacted with 100% H_3PO_4 at 60°C under vacuum conditions, producing CO_2 that was measured using a Finnigan MAT 253 mass spectrometer. Results were calibrated to the V-PDB standard, with reproducibility <0.1‰, monitored by replicate analysis of standards (GBW 04416, GBW 04417; $n = 21$).

For pyrite framboid size analysis, 51 thin sections were examined using a Hitachi SU8010 scanning electron microscope at 2,500X magnification in backscattered electron mode. For Fe proxies to be considered reliable in paleoredox analysis, samples with a total Fe content (Fe_T) > 0.5 wt% were selected (Clarkson et al., 2014). The Fe_T contents were determined on bulk rock samples using X-ray fluorescence spectroscopy, with a reproducibility better than 0.1 wt% (1σ). The sequential extraction process, following the protocol of Poulton and Canfield (2005), allows for the quantification of highly reactive Fe (Fe_{HR}) including carbonate-associated Fe, "easily reducible" oxyhydroxides, ferric iron (oxyhydr)oxides, and magnetite. The iron content in the form of pyrite (Fe_{Py}) was determined through chromium reduction (Canfield et al., 1986).

4. Results

4.1. Sedimentary Facies

The lower part of the exposed Wuchiaping Formation at Ruichang consists of ∼10 m of medium- to thickly-bedded gray grainstones, packstones and wackestones. Grainstones, observed only within an interval of ∼65 cm of strata in the lower part of the Wuchiaping Formation, contain abundant echinoderms, foraminifera, and calcareous algae, as well as rarer ostracods, brachiopods and gastropods (Figure 3a). Packstones seen in the lower part of the Wuchiaping Formation become less common upsection, where wackestones dominate. Packstones and wackestones are intensively bioturbated and contain diverse and abundant bioclasts (Figures 3b and 3j–3n). The overlying Talung Formation consists mostly of thinly-bedded cherts, siliceous wackestones, black shales, and marls (Figure 2a). Cherts are most common in the basal part of this unit. Black shale partings separate the siliceous wackestones. Faunal abundance and diversity decrease significantly in this unit compared to the Wuchiaping Formation, with a prominent shift in fossil assemblages from calcareous benthic organisms to predominantly siliceous taxa including radiolarians and sponges (Figure 3c). The uppermost ∼1 m of the Talung Formation comprises an intraclastic (peloidal) wackestone (Figure 3d) interbedded with siliceous wackestone. The succeeding Lower Triassic Daye Formation is characterized by thinly-bedded wackestones and marls containing abundant bivalves (belonging to the "disaster taxon" *Claraia*) and ammonoids (*Ophiceras*) (Figures 2a–2d).

At Ehtan, the uppermost Heshan Formation features ∼65 cm of intensively bioturbated wackestones with chert nodules, and is rich in bioclasts, including calcareous sponges, gastropods, brachiopods and calcareous algae (Figure 3e). The overlying Talung Formation is dominated by thinly-bedded siliceous wackestones and packstones, along with interbedded cherts, marls, mudstones, and sandstones (Figures 2e and 3f–3h). Bedded cherts mainly occur in the middle of this unit, with mudstones and sandstones prevalent in the upper part. The Talung Formation is notably rich in siliceous fossils, while calcareous fossils like ammonoids are rare, occurring mainly in the upper part (Figures 2g and 2h). Only the lowermost ∼1.8 m of the Luolou Formation is exposed at Ehtan, where it comprises light brown, thinly bedded and finely laminated mudstones (Figure 2f). *Claraia* is seen at ∼1 m above the base of this formation.
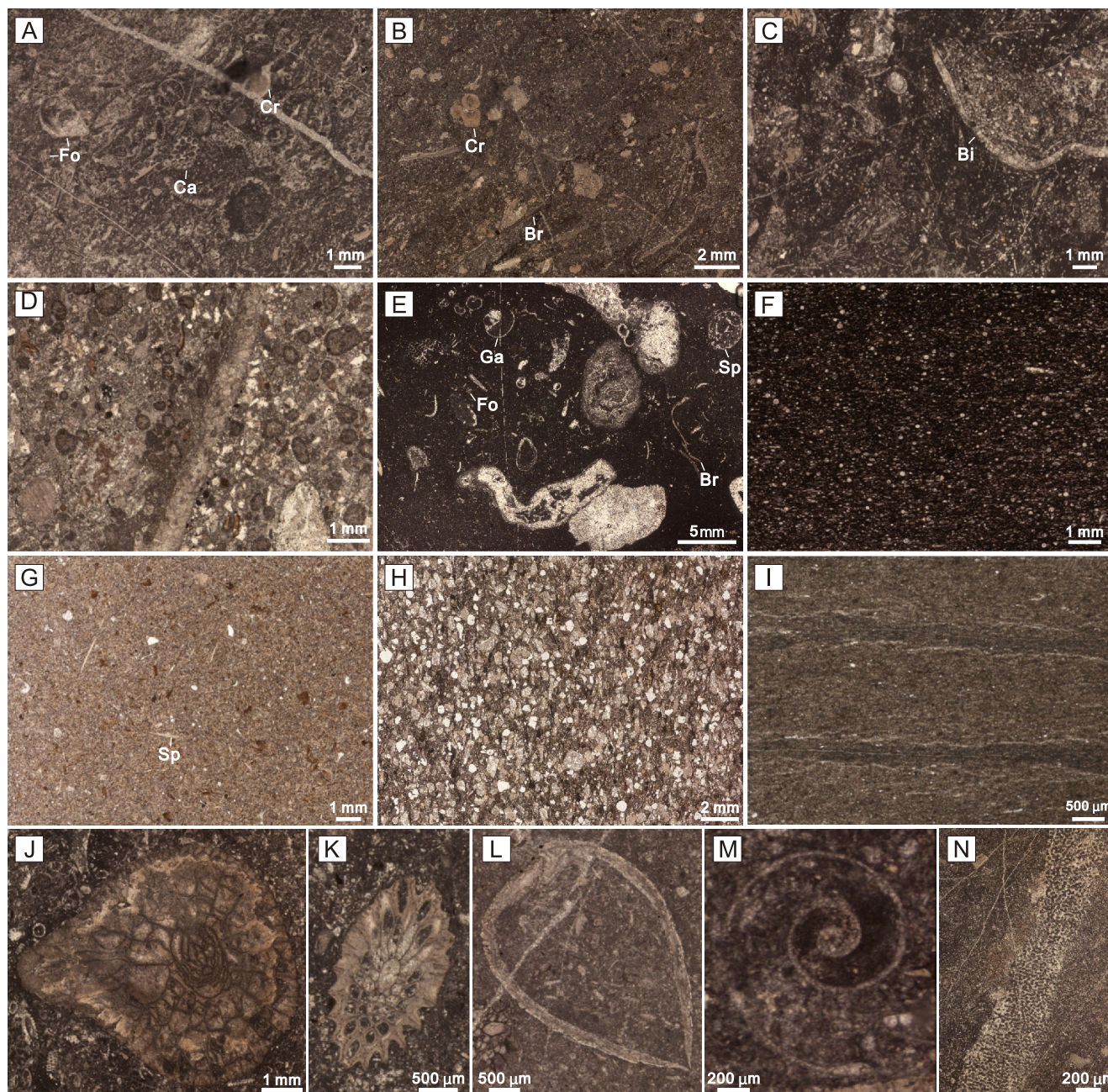
Figure 3. Photomicrographs of samples from the Ruichang (a–d, j–n) and Ehtan (e–i) sections. (a) Grainstone with crinoids (Cr), foraminifers (Fo) and calcareous algae (Ca) from the lower Wuchiaping Formation; (b) Crinoid (Cr) wackestone with brachiopods (Br) from the lower Wuchiaping Formation; (c) Packstone with radiolarians, sponge spicules and bivalves (Bi) from the upper Talung Formation; (d) Wackestone with peloidal intraclast in the uppermost Talung Formation; (e) Calcareous sponge (Sp) wackestone with foraminifers (Fo), gastropods (Ga) and brachiopods (Br) from the upper Heshan Formation; (f) Radiolarite from the middle Talung Formation; (g) Wackestone with sponge spicules (Sp) from the upper Talung Formation; (h) Sandstone from the upper Talung Formation; (i) Non-bioturbated mudstone showing fine lamination from the lower Luolou Formation; (j) Coral (*Syringopora*); (k) Bryozoan; (l) Brachiopod; (m) Gastropod; (n) Calcareous sponge.

4.2. Carbon Isotope Composition ($\delta^{13}C_{carb}$)

At Ruichang, $\delta^{13}C_{carb}$ values in the Wuchiaping Formation range from 2.0 to 3.5‰. A prominent negative excursion of −4.1‰ (from 3.0‰ to −1.1‰) occurs at the Wuchiaping-Talung transition. In the lower Talung Formation, $\delta^{13}C_{carb}$ values fluctuate around −1.0‰ before recovering to 0.6‰ upsection. This is followed by a second negative excursion of −3.9‰ (from 0.6‰ to −3.3‰) in the uppermost Talung Formation. Upsection, $\delta^{13}C_{carb}$ values rise through the lower part of the Daye Formation (Figure 4).
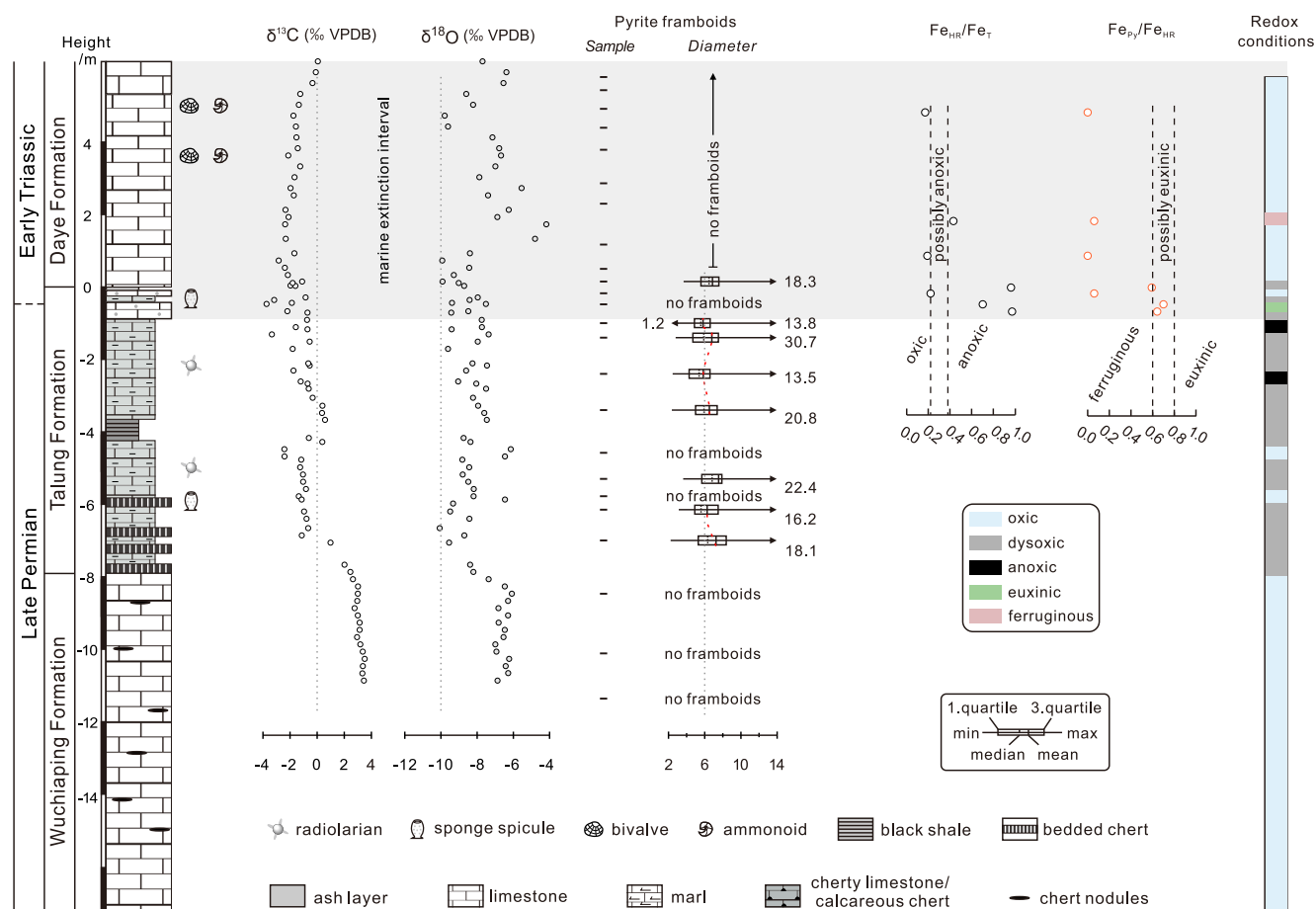
Figure 4. Stratigraphic log of the Ruichang section with $\delta^{13}C_{carb}$, $\delta^{18}O_{carb}$, iron phase partitioning proxy data, and pyrite framboid "box-and-whisker" plots. Redox conditions are inferred from framboid sizes and iron proxies, with consideration of bioturbation intensity and fossil occurrences (see Section 5.3). The marine extinction interval shown in this figure is based on that at the Meishan section (S. Shen et al., 2011).

At Ehtan, $\delta^{13}C_{carb}$ values fluctuate around 2.0‰ at the top of the Heshan Formation (Figure 5). The $\delta^{13}C_{carb}$ record includes a negative shift of −2.3‰ (from 1.8‰ to −0.5‰) across the Heshan-Talung contact. The majority of the $\delta^{13}C_{carb}$ values in the Talung Formation range from −2.0‰ to 0‰, with a few falling between 0 and 2‰. After rebounding from the first excursion, $\delta^{13}C_{carb}$ values display a second negative excursion of −2.8‰ (from −0.6‰ to −3.4‰) at the top of the Talung Formation (Figure 5). No $\delta^{13}C_{carb}$ data is available for the basal Daye Formation due to its low carbonate content.

4.3. Pyrite Framboid Analysis

Pyrite framboids are generally absent in the Wuchiaping and Heshan Formations but are common in the Talung Formation. These framboids exhibit typical early diagenetic characteristics in terms of size and morphology (e.g., Wignall & Newton, 1998; Figure 6). At Ruichang, mean framboid diameters (MFDs) range from 5.8 to 7.3 µm in the Talung Formation (Figure 4) with standard deviations (SDs) between 1.4 and 3.2 µm (Figure 7, Table S1 in Supporting Information S1). Pyrite framboids are absent in several siliceous beds in the lower Talung Formation and the uppermost ~1 m intraclastic (peloidal) wackestone. Abundant framboids are seen at the base of the Daye Formation, where they have an MFD of 6.7 µm and an SD of 1.6 µm. Other than this level, the lower part of the Daye Formation lacks framboids.

At Ehtan, the MFDs ranged from 6.1 to 10.7 µm in the Talung Formation (Figure 5), with SDs from 2.2 to 6.6 µm (Figure 7, Table S1 in Supporting Information S1). Pyrite framboids are absent in the middle part of the Talung Formation and are rare in the upper Talung Formation. In the lower Luolou Formation post-extinction strata, only
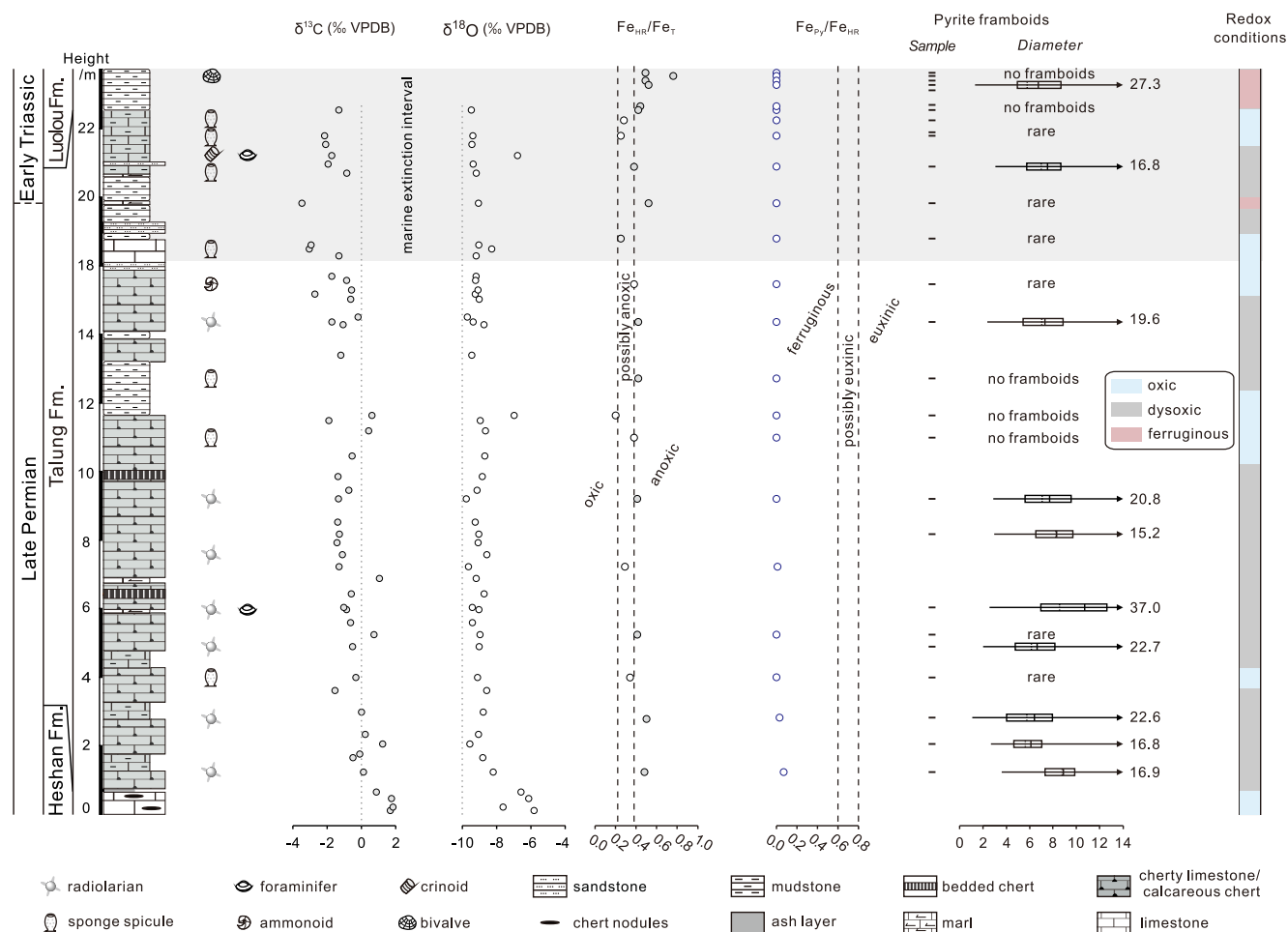
Figure 5. Stratigraphic log of the Ehtan section with $\delta^{13}C_{carb}$, $\delta^{18}O_{carb}$, iron phase partitioning proxy data, and pyrite framboid "box-and-whisker" plots. Fm = formation. Redox conditions are inferred from framboid sizes and iron proxies, with consideration of bioturbation intensity and fossil occurrences (see Section 5.3).

Figure 6. SEM images of pyrite in samples from the Ruichang and Ehtan sections. (a) Euhedral and framboidal pyrite from the upper Talung Formation of the Ruichang section; (b) Euhedral and framboidal pyrite from the lower Talung Formation of the Ehtan section.

Figure 7. Mean diameter versus standard deviation for pyrite framboid populations measured in the studied samples. The dashed line separates euxinic from suboxic–oxic fields based on modern/experimental work (cf., Wilkin et al., 1996).
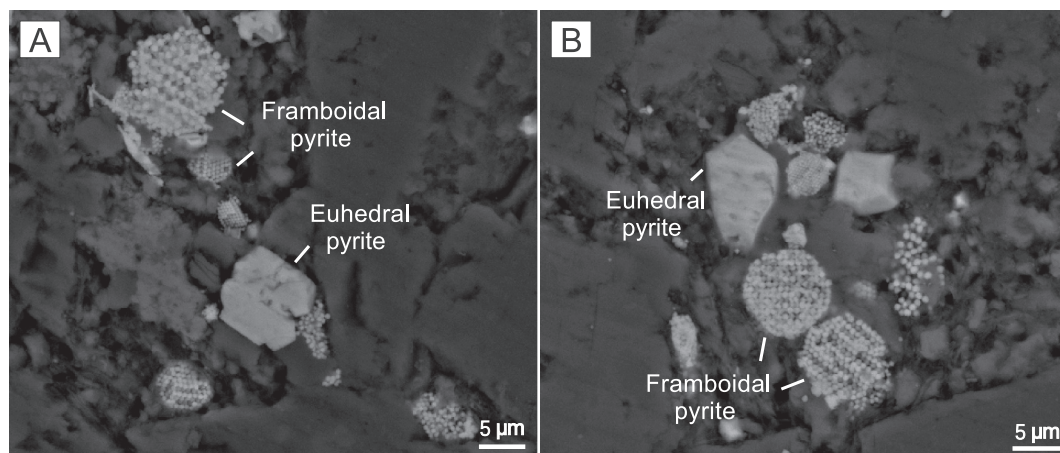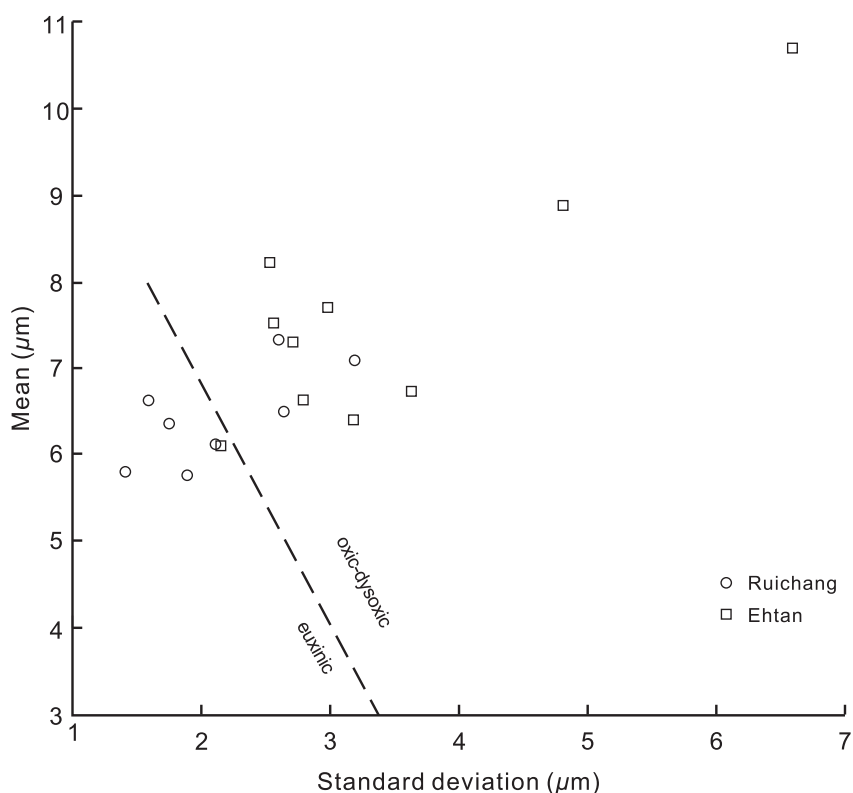
one sample contained abundant pyrite framboids, with an MFD of 6.7 μm and an SD of 3.6 μm. Pyrite framboids were absent in the remaining beds.

4.4. Iron Phase Partitioning

At Ruichang, a decrease in the reactive iron to total iron ratio (Fe_{HR}/Fe_T) is seen at the Talung-Daye transition. Fe_{HR}/Fe_T first decreases from 0.97 to 0.22 before returning to a value of 0.96 at the level at which siliceous organisms disappear. Thereafter, this ratio maintains low values in the interval where pyrite framboids are absent (Figure 4). The pyrite iron to reactive iron ratio (Fe_{Py}/Fe_{HR}) exhibits a similar trend in which Fe_{Py}/Fe_{HR} declines from 0.69 to 0.06 before rising again to 0.59 at the siliceous organism extinction level. Fe_{Py}/Fe_{HR} ratio is consistently low in the basal Daye Formation.

At Ehtan, the Fe_{HR}/Fe_T ratio is between 0.20 and 0.52 in the Talung Formation (Figure 5) and exhibits an increase from 0.25 to 0.44 at the Talung-Luolou transition. Fe_{HR}/Fe_T ratios are between 0.44 and 0.76 in the lower Luolou Formation. Fe_{Py}/Fe_{HR} ratios are consistently low in this section, with most samples having values of zero, and the maximum Fe_{Py}/Fe_{HR} value being 0.07.

5. Discussion

5.1. Sedimentary Environments

At Ruichang, the common calcareous algae in grainstones of the Wuchiaping Formation suggest deposition within the euphotic zone (Flügel, 2010). Packstones and wackestones dominate the middle Wuchiaping Formation, where echinoderms constitute the principal bioclasts. Foraminifera, brachiopods and gastropods are common, accompanied by less common corals, bryozoans, sponges, and ostracods. The scarce and fragmented nature of calcareous algae suggests that they have been transported from a nearby platform rather than being deposited in situ. The wackestones of the upper Wuchiaping Formation contain brachiopods and crinoids along with rarer foraminifera, ostracods, bryozoans, and sponges. Notably, these strata lack calcareous algae,

suggesting a progressive deepening toward a middle to lower ramp setting within the Wuchiaping Formation (Flügel, 2010). In the overlying Talung Formation, the replacement of calcareous bioclasts with siliceous bioclasts in thinly-bedded black shales and cherts suggests further deepening into a basinal setting. In the lower Daye Formation, finely laminated wackestones/marls with abundant and well-preserved ammonoids and bivalves (*Claraia*) also point toward a relatively deep-water environment.

At Ehtan, the upper Heshan Formation is dominated by wackestones with abundant calcareous sponges, brachiopods and sporadic occurrences of foraminifera, gastropods, bryozoans, and algal fragments, suggesting a middle to lower ramp environment (Flügel, 2010). The Heshan-Talung transition sees siliceous sponge spicules and radiolarians come to dominate the fossil assemblages, indicating significant drowning and the development of a basinal setting. The overlying lower Luolou Formation comprises finely laminated mudstones with intact *Claraia* shells, documenting a low-energy deep-water environment similar to that in which the Daye Formation was deposited at Ruichang.

5.2. $\delta^{13}C_{carb}$ Records From the Late Permian to the Early Triassic

Post-depositional processes could potentially alter the original $\delta^{13}C_{carb}$ signature of marine carbonates (e.g., Hayes et al., 1999; Kaufman & Knoll, 1995). Generally, $\delta^{18}O_{carb} < -10‰$ may indicate significant diagenetic alteration (Kaufman & Knoll, 1995). In this study, only one out of 132 samples shows $\delta^{18}O_{carb} < -10‰$ (Figure 4). Additionally, a positive correlation between $\delta^{13}C_{carb}$ and $\delta^{18}O_{carb}$ is often used as an indicator of diagenetic effects (e.g., Derry, 2010; Knauth & Kennedy, 2009). In our study, $\delta^{13}C_{carb}$ and $\delta^{18}O_{carb}$ from both sections were not significantly correlated ($r^2 = 0.12$ and 0.31, respectively).

Both study sections recorded a negative $\delta^{13}C_{carb}$ excursion near the Wuchiapingian-Changhsingian boundary. Despite being well-documented in South China (e.g., L. J. Li et al., 2020; S. Z. Shen et al., 2013), this excursion is not clearly expressed in other regions, hindering global correlation of this level. For instance, shallow-water carbonate successions in Armenia and Iran reveal no excursion across this transition (e.g., Gliwa et al., 2020; Joachimski et al., 2020). Limited conodont data suggest the Wuchiapingian-Changhsingian excursion is diachronous, with its minimum value reached between the *C. orientalis* and *C. subcarinata* zones (S. Z. Shen et al., 2013; F. Yang et al., 2022). Moreover, the magnitude of this excursion varies considerably, ranging from a modest shift of 2.3‰ to a major shift of 6.3‰, complicating the application of $\delta^{13}C_{carb}$ chemostratigraphic correlation for this interval.

The late Changhsingian $\delta^{13}C_{carb}$ values in South China demonstrate depth-dependent variation. $\delta^{13}C_{carb}$ values of ~0‰ at Ruichang and Ehtan contrast with heavier values in lower slope/basinal sections like Chibi (~2.5‰), and even heavier values from platform sections (~4‰) (e.g., Korte & Kozur, 2010; Luo et al., 2011; Xie et al., 2007). This suggests that an active biological pump depleted ^{12}C in the surface dissolved inorganic carbon pool.

Extensive research has identified significant carbon cycle perturbations across the P-T boundary, primarily manifesting as a pronounced negative $\delta^{13}C_{carb}$ shift that is recognized worldwide, albeit with spatial heterogeneity (e.g., Holser et al., 1991; Musashi et al., 2001; Payne et al., 2004). The basinal sites at Chibi (facing Tethys) and Ehtan (facing Panthalassa) record a negative $\delta^{13}C_{carb}$ excursion of −2.8‰ (F. Yang et al., 2022), faithfully replicating other boundary $\delta^{13}C_{carb}$ records. The P-T boundary in both study sections is placed at the top of the Talung Formation, using $\delta^{13}C_{carb}$ chemostratigraphic correlation (Korte & Kozur, 2010; Figures 4 and 5).

5.3. Redox Evolution and Its Implication for the EPME

Iron petrography and geochemistry are widely applied to marine sedimentary successions as redox proxies. The absence or rarity of pyrite framboids is often invoked as indicative of oxic seafloor conditions (Bond & Wignall, 2010). Large populations of small framboids (MFDs ~4–6 μm) reflect anoxic/euxinic conditions, while populations of larger framboids (MFDs ~6–10 μm) indicate dysoxic conditions (Bond & Wignall, 2010). The ratios of Fe_{HR}/Fe_T and Fe_{Py}/Fe_{HR} are used to differentiate between oxic, ferruginous and euxinic conditions (Poulton & Canfield, 2011). Specifically, $Fe_{HR}/Fe_T < 0.22$ indicates well-oxygenated environments, while values >0.38 are associated with anoxic conditions. The ratios between these values are equivocal regarding the redox state. Ratios of $Fe_{Py}/Fe_{HR} < 0.6$ indicate ferruginous environments, while those between 0.6 and 0.8 are considered to reflect possibly euxinic conditions, and ratios >0.8 are associated more conclusively with euxinia (Poulton, 2021).

The combined redox proxies for Ruichang and Ehtan indicate that fully oxygenated conditions developed throughout the deposition of the Wuchiaping and Heshan Formations, consistent with the abundance of benthic fossils and high degree of bioturbation (Figures 4 and 5). The Talung Formation at Ruichang has framboid populations with MFDs of 6–8 μm, suggesting that dysoxic conditions were interrupted by episodic anoxia, indicated by the MFDs of ∼5.8 μm at a section height of −1 m. At the level at which siliceous organisms disappear, elevated Fe_{HR}/Fe_T and Fe_{Py}/Fe_{HR} ratios, together with the presence of populations of small pyrite framboids, indicate the onset of dysoxic conditions. Meanwhile, Ehtan records sustained dysoxic depositional conditions that were punctuated by frequent oxic and brief ferruginous pulses. Pyrite framboids are absent in strata deposited under both oxic and ferruginous conditions. Oxic conditions are inferred from low Fe_{HR}/Fe_T values and the abundance of benthic organisms (Figure 5). In contrast, ferruginous conditions are marked by high Fe_{HR}/Fe_T values, low Fe_{Py}/Fe_{HR} values, and the absence of benthic organisms.

Above the horizon at which siliceous organisms disappear, the lowermost 3.9 m of the Daye Formation at Ruichang documents oxic depositional conditions on the basis of the low Fe_{HR}/Fe_T ratios at that level (also characterized by a lack of pyrite framboids; Figure 4). Only one sample from the Daye Formation has a moderately elevated Fe_{HR}/Fe_T value (0.4), suggesting a possible short-lived ferruginous pulse. The overlying strata contain common *Claraia* and *Ophiceras*. *Claraia*, a taxon that flourished after the EPME, thrived in a wide range of conditions, spanning oxic to oxygen-restricted settings (Wignall & Hallam, 1992; H. Yang et al., 2021). At Ruichang, *Claraia* inhabited an oxygenated seafloor, while *Ophiceras* occupied an oxygenated water column.

At Ehtan, the Talung-Luolou transition is marked by a decrease in oxygen levels. The uppermost Talung Formation records oxic conditions, as indicated by rare framboids, a decline in Fe_{HR}/Fe_T, and an abundant benthic fauna (Figure 5; Poulton, 2021). In contrast, the lowermost Luolou Formation is characterized by ferruginous conditions, evidenced by the framboid gap, high Fe_{HR}/Fe_T ratios, low Fe_{Py}/Fe_{HR} ratios, and the absence of benthic fossils (Figure 5). *Claraia*'s presence in oxygen-limited environments aligns with its known tolerance for dysoxic conditions (Wignall & Hallam, 1992).

Anoxia (including euxinic and ferruginous conditions) contributed to mortality among marine benthic organisms during the EPME (e.g., Clarkson et al., 2016; Meyer et al., 2008; Wignall & Hallam, 1992). Proxy records in the Ruichang and Ehtan sections show dynamic redox changes across the P-T boundary beds. At Ruichang, the dysoxic-anoxic intervals are intercalated with oxic periods during the extinction interval. Massive accumulation of free H_2S in both shallow and deep settings has been postulated as a kill mechanism for the EPME (e.g., Grice et al., 2005; Nielsen & Shen, 2004). However, iron proxies from Ehtan show no support for this scenario. High Fe_{HR}/Fe_T ratios (>0.38) and low Fe_{Py}/Fe_{HR} ratios (<0.6) indicate a ferruginous condition with limited free H_2S in the water column (Poulton, 2021). These non-sulfidic (ferruginous) conditions were widespread during the P-T transition and in the Early Triassic (e.g., Clarkson et al., 2016; Xiang et al., 2016, 2020). Unlike sulfidic conditions, where enhanced phosphorus is regenerated at the sediment-water interface and promotes primary productivity (Cappellen & Ingall, 1996), ferruginous conditions regulate the phosphorus cycle through interplays with the Fe cycle. Fe (oxy)hydroxides scavenge reactive phosphorus in the water column (e.g., Guilbaud et al., 2020; Reinhard et al., 2017), lowering the ocean's primary productivity and causing the collapse of marine food webs (e.g., X. T. Ge et al., 2022; Müller et al., 2022; Sun, 2024; Woods et al., 2023).

5.4. Spatial and Temporal Variations in P-T Oceanic Redox Conditions

A substantial body of research evaluating oceanic redox changes across the P-T boundary has revealed marked redox heterogeneity, especially in basins within the SCB (e.g., Cao et al., 2009; Wignall et al., 1995). The low Fe_{HR}/Fe_T ratios (<0.22) at Ruichang point to the re-emergence of oxygenated conditions during the EPME in the north marginal basin of the Yangtze Platform. Conversely, high Fe_{HR}/Fe_T ratios (>0.38), and low Fe_{Py}/Fe_{HR} (<0.6) at Ehtan indicate ferruginous conditions in the Lower Triassic within the Xiang-Qian-Gui Basin. A framboid gap—of differing origin—is seen in both records.

Iron proxies reveal dynamic shifts from euxinic to ferruginous conditions in the north marginal basin of the Yangtze Platform. These changes were slightly diachronous but can be divided into three phases. In Phase 1, the early Changhsingian (*C. wangi* to *C. changxingensis* zones) marked the establishment of euxinia along the lower slopes and in basinal settings (Figure 8a; Lei et al., 2017; Xiang et al., 2016), contrasting with dysoxic to oxic conditions on platforms and along the upper slopes where calcareous taxa flourished (Jin et al., 2006). Phase 2, during the late Changhsingian (*C. yini* to *H. praeparvus* zones) is marked by the upward expansion of euxinic waters into slope
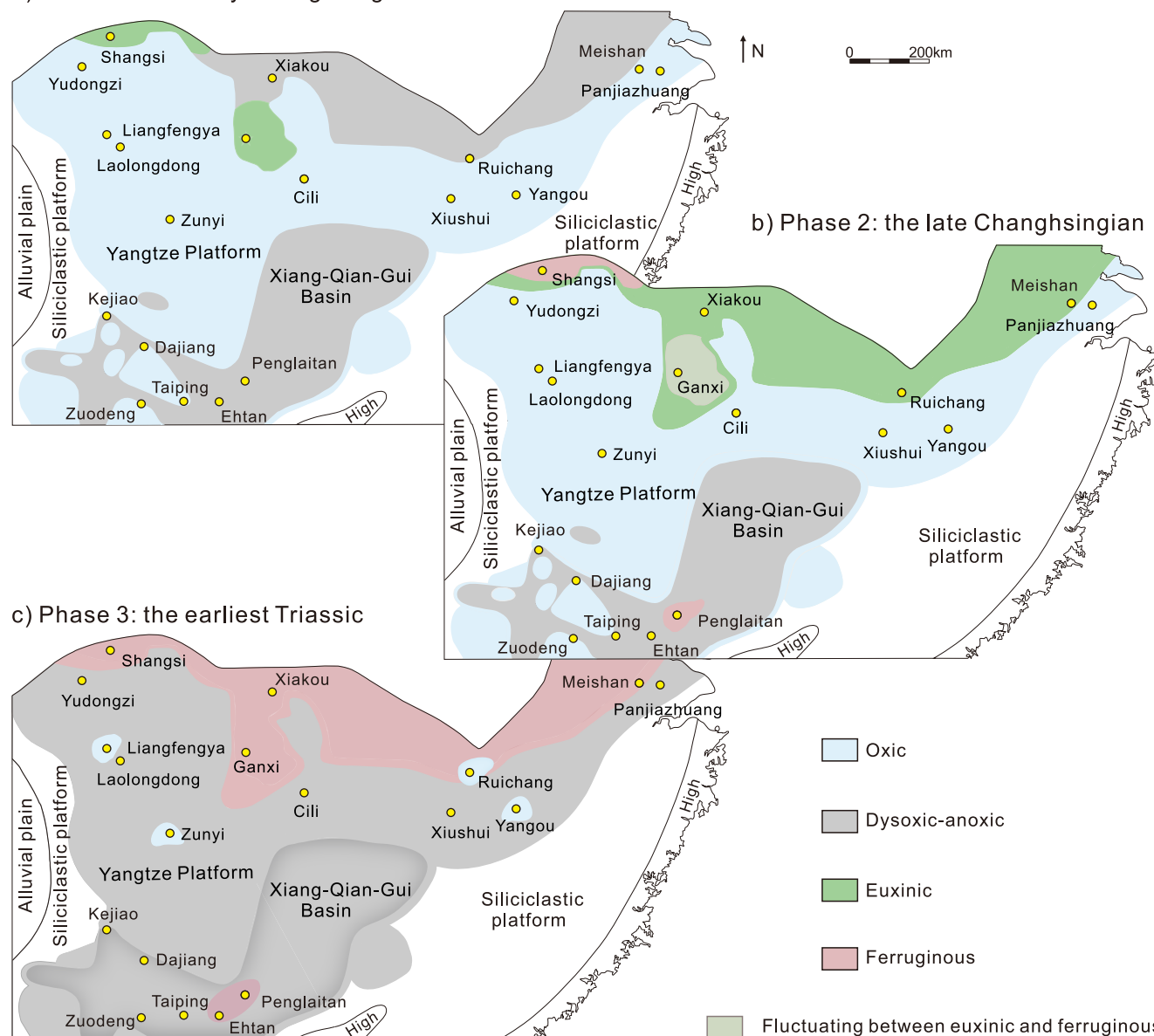
Figure 8. Redox evolution through the P-T transition in South China. (a) Phase 1: the early Changhsingian; (b) Phase 2: the late Changhsingian; (c) Phase 3: the earliest Triassic. Data sources: Xiakou: S. Shen et al. (2011); Shangsi: Xiang et al. (2016); Ganxi: Lei et al. (2017); Xiushui: Wu et al. (2017); Cili and Taiping: Xiao et al. (2018); Panjiazhuang: Huang et al. (2019); Meishan: Xiang et al. (2020); Zunyi, Liangfenya, Dajiang, Yudongzi, and Yangou: Chen et al. (2022); Kejiao: Wang et al. (2023).

environments, while euxinia was locally replaced by ferruginous conditions, during a time of global warming and carbon cycle disturbances (Figure 8b; Sun et al., 2012). This interval also experienced a weakening in ocean circulation and increased stratification that exacerbated oxygen-restriction in the water column. Phase 3, in the earliest Triassic period saw ferruginous conditions expand further and occupy both slope and basinal environments. Sporadic euxinia and brief oxygenation events also characterize this interval (Figure 8c).

5.5. The Framboid Gap: Extent and Genesis

The P-T framboid gap appears to be transient, regional, and diachronous. The earliest onset of the framboid gap began in the lowermost Triassic *H. parvus* Zone in this study. Its maximum temporal extent, as seen at Chibi, is from the latest Permian *C. yini-H. praeparvus* Zone to the Early Triassic *I. isarcica* Zone (F. Yang et al., 2022). At most

sites, the framboid gap is constrained to the *H. parvus* Zone within the P-T marine extinction interval and it is most pronounced in slope to basinal settings along the north marginal basin of the Yangtze Platform (Chen et al., 2022).

The genesis of authigenic pyrite is governed by sulfate concentration (Berner, 1984), which was reportedly lower than 1 mM in the P-T oceans (Luo et al., 2010), although higher concentrations (2–6 mM) have also been postulated (Bernasconi et al., 2017). An alternative explanation lies in the supply of decomposable organic matter (Berner, 1984). Previous studies on phosphorus speciation and nickel concentrations suggest a decline in productivity across the Tethys and Panthalassa realms between the latest Permian and the Early Triassic (Müller et al., 2022; Woods et al., 2023), coinciding with the demise of chert deposition in the region (F. Yang et al., 2022). A collapse in primary productivity in the surface oceans would have curtailed the influx of organic matter, thereby restricting sulfate reduction and subsequent pyrite formation. It is notable that the framboid gap has not been reported in better-ventilated P-T boundary microbialites.

Improved ocean ventilation has been invoked as the underlying driver of the framboid gap, but the mechanism by which a thermally stratified and highly anoxic ocean is ventilated is not fully understood. Our multi-proxy study lends some support to the ventilation theory but also highlights a reduction in primary production as a key factor in transient ocean re-oxygenation episodes. However, the framboid gap in strata that were likely deposited under ferruginous conditions in South China highlights the intricate nature of redox shifts during the EPME. In the period leading up to and following the mass extinction, global warming likely enhanced ocean stratification and curtailed the upwelling of nutrient-rich waters, exacerbating losses in biomass. This decrease in productivity, in turn, would have lowered marine oxygen demand for organic matter respiration and decomposition, thereby aiding in the gradual replenishment of dissolved oxygen in seawater.

6. Conclusions

Paleontological, sedimentological, and geochemical analyses of sections in South China shed light on Late Permian and Early Triassic environmental shifts in epicontinental basins. Variations in pyrite framboid size, iron phase partitioning, and bioturbation intensities suggest the prevalence of dysoxic conditions interspersed with short-lived anoxic (euxinic/ferruginous) events and better oxygenated periods in the Late Permian. Early Triassic redox conditions display notable spatial variability, though the "framboid gap" occurred in South China. Iron phase partition points to the development of both oxic and ferruginous environments in the north marginal basin of the Yangtze Platform, while ferruginous conditions prevailed in the contemporaneous Xiang-Qian-Gui Basin.

The "framboid gap" is probably a function of reduced primary productivity in the eastern Tethys ocean, where limited organic matter input curtailed sulfate reduction, and thus restricted framboid growth. While pyrite framboid morphology remains a critical indicator for reconstructing past redox settings, it is critical to acknowledge that the absence of framboids does not necessarily document a well oxygenated environment as often inferred: their absence can also indicate ferruginous conditions. This has great significance for the interpretation of pyrite framboid size populations as a redox proxy.

Nevertheless, the development of oxygenated conditions in the end-Permian marine extinction interval in South China highlights the dynamic nature of Permian-Triassic ocean anoxia.

Data Availability Statement

All supplementary data related to this paper are available at F. Yang et al. (2024).

References

Beatty, T. W., Zonneveld, J. P., & Henderson, C. M. (2008). Anomalously diverse Early Triassic ichnofossil assemblages in Northwest Pangea: A case for a shallow-marine habitable zone. *Geology*, *36*(10), 771–774. https://doi.org/10.1130/g24952a.1

Bernasconi, S. M., Meier, I., Wohlwend, S., Brack, P., Hochuli, P. A., Bläsi, H., et al. (2017). An evaporite-based high-resolution sulfur isotope record of Late Permian and Triassic seawater sulfate. *Geochimica et Cosmochimica Acta*, *204*, 331–349. https://doi.org/10.1016/j.gca.2017.01.047

Berner, R. A. (1984). Sedimentary pyrite formation: An update. *Geochimica et Cosmochimica Acta*, *48*(4), 605–615. https://doi.org/10.1016/0016-7037(84)90089-9

Bond, D. P. G., & Wignall, P. B. (2010). Pyrite framboid study of marine Permian-Triassic boundary sections: A complex anoxic event and its relationship to contemporaneous mass extinction. *Geological Society of America Bulletin*, *122*(7–8), 1265–1279. https://doi.org/10.1130/B30042.1

Canfield, D. E., Raiswell, R., Westrich, J. T., Reaves, C. M., & Berner, R. A. (1986). The use of chromium reduction in the analysis of reduced inorganic sulfur in sediments and shales. *Chemical Geology*, *54*(1–2), 149–155. https://doi.org/10.1016/0009-2541(86)90078-1

Cao, C. Q., Love, G. D., Hays, L. E., Wang, W., Shen, S. Z., & Summons, R. E. (2009). Biogeochemical evidence for euxinic oceans and ecological disturbance presaging the end-Permian mass extinction event. *Earth and Planetary Science Letters*, *281*(3–4), 188–201. https://doi.org/10.1016/j.epsl.2009.02.012

Cappellen, P. V., & Ingall, E. D. (1996). Redox stabilization of the atmosphere and oceans by phosphorus-limited marine productivity. *Science*, *271*(5248), 493–496. https://doi.org/10.1126/science.271.5248.493

Chen, Z. Q., Fang, Y. H., Wignall, P. B., Guo, Z., Wu, S. Q., Liu, Z. L., et al. (2022). Microbial blooms triggered pyrite framboid enrichment and oxygen depletion in carbonate platforms immediately after the latest Permian extinction. *Geophysical Research Letters*, *49*(7), 11. https://doi.org/10.1029/2021gl096998

Clarkson, M. O., Poulton, S. W., Guilbaud, R., & Wood, R. A. (2014). Assessing the utility of Fe/Al and Fe-speciation to record water column redox conditions in carbonate-rich sediments. *Chemical Geology*, *382*, 111–122. https://doi.org/10.1016/j.chemgeo.2014.05.031

Clarkson, M. O., Wood, R. A., Poulton, S. W., Richoz, S., Newton, R. J., Kasemann, S. A., et al. (2016). Dynamic anoxic ferruginous conditions during the end-Permian mass extinction and recovery. *Nature Communications*, *7*(1), 12236. https://doi.org/10.1038/ncomms12236

Dal Corso, J., Song, H. J., Callegaro, S., Chu, D. L., Sun, Y. D., Hilton, J., et al. (2022). Environmental crises at the Permian-Triassic mass extinction. *Nature Reviews Earth & Environment*, *3*, 197–214. https://doi.org/10.1038/s43017-021-00259-4

Derry, L. A. (2010). A burial diagenesis origin for the Ediacaran Shuram-Wonoka carbon isotope anomaly. *Earth and Planetary Science Letters*, *294*(1–2), 152–162. https://doi.org/10.1016/j.epsl.2010.03.022

Feng, Z. Z., Yang, Y. Q., Jin, Z. K., He, Y. B., Wu, S. H., Xin, W. J., et al. (1996). Lithofacies paleogeography of the Permian of South China. *Acta Sedimentologica Sinica*, *14*(2), 1–11. (in Chinese with English abstract). https://doi.org/10.14027/j.cnki.cjxb.1996.02.001

Flügel, E. (2010). Depositional models, facies zones and standard microfacies. *Microfacies of carbonate rocks: Analysis, interpretation and application* (pp. 657–724).

Ge, X. T., Chen, D. Z., Zhang, G. J., Huang, T. Y., Liu, M., & El-Shafeiy, M. (2022). Marine redox evolution and organic accumulation in an intrashelf basin, NE Sichuan Basin during the Late Permian. *Marine and Petroleum Geology*, *140*, 105633. https://doi.org/10.1016/j.marpetgeo.2022.105633

Ge, Y. Z., & Bond, D. P. G. (2022). Two deep marine oxygenation events during the Permian-Triassic boundary interval in South China: Relationship with ocean circulation and marine primary productivity. *Earth-Science Reviews*, *234*, 104220. https://doi.org/10.1016/j.earscirev.2022.104220

Gliwa, J., Ghaderi, A., Leda, L., Schobben, M., Tomás, S., Foster, W. T., et al. (2020). Aras Valley (northwest Iran): High-resolution stratigraphy of a continuous central Tethyan Permian–Triassic boundary section. *Fossil Record*, *23*(1), 33–69. https://doi.org/10.5194/fr-23-33-2020

Golonka, J. (2002). Plate-tectonic maps of the Phanerozoic. In W. Kiessling, E. Flügel, & J. Golonka (Eds.), *Phanerozoic Reef Patterns* (Vol. 72, pp. 21–76). SEPM Special Publication.

Grasby, S. E., Bond, D. P. G., Wignall, P. B., Yin, R., Strachan, L. J., & Takahashi, S. (2021). Transient Permian-Triassic euxinia in the southern Panthalassa deep ocean. *Geology*, *49*, 889–893. https://doi.org/10.1130/g48928.1

Grice, K., Cao, C. Q., Love, G. D., Bottcher, M. E., Twitchett, R. J., Grosjean, E., et al. (2005). Photic zone euxinia during the Permian–Triassic superanoxic event. *Science*, *307*(5710), 706–709. https://doi.org/10.1126/science.1104323

Guilbaud, R., Poulton, S. W., Thompson, J., Husband, K. F., Zhu, M., Zhou, Y., et al. (2020). Phosphorus-limited conditions in the early Neoproterozoic ocean maintained low levels of atmospheric oxygen. *Nature Geoscience*, *13*(4), 236–301. https://doi.org/10.1038/s41561-020-0548-7

Hayes, J. M., Strauss, H., & Kaufman, A. J. (1999). The abundance of ^{13}C in marine organic matter and isotopic fractionation in the global biogeochemical cycle of carbon during the past 800 Ma. *Chemical Geology*, *161*(1–3), 103–125. https://doi.org/10.1016/S0009-2541(99)00083-2

Holser, W. T., Schönlaub, H. P., Boeckelmann, K., Magaritz, M., & Orth, C. J. (1991). The Permian-Triassic of the Gartnerkofel-1 core (Carnic Alps, Austria): Synthesis and conclusions. *Abhandlungen der Geologischen Bundesanstalt*, *45*, 213–235.

Huang, Y. F., Bond, D. P. G., Wang, Y. B., Wang, T., Yi, Z. X., Yuan, A. H., et al. (2019). Early Triassic microbialites from the Changxing Region of Zhejiang Province, South China. *Journal of Palaeogeography*, *8*(1), 22. https://doi.org/10.1186/s42501-019-0039-1

Jin, Y. G., Wang, Y., Henderson, C., Wardlaw, B. R., Shen, S. Z., & Cao, C. Q. (2006). The Global Boundary Stratotype Section and Point (GSSP) for the base of Changhsingian Stage (Upper Permian). *Episodes*, *29*(3), 175–182. https://doi.org/10.18814/epiiugs/2006/v29i3/003

Joachimski, M. M., Alekseev, A. S., Grigoryan, A., & Gatovsky, Y. A. (2020). Siberian Trap volcanism, global warming and the Permian-Triassic mass extinction: New insights from Armenian Permian-Triassic sections. *Geological Society of America Bulletin*, *132*(1–2), 427–443. https://doi.org/10.1130/b35108.1

Kaufman, A. J., & Knoll, A. H. (1995). Neoproterozoic variations in the C-isotopic composition of seawater: Stratigraphic and biogeochemical implications. *Precambrian Research*, *73*(1–4), 27–49. https://doi.org/10.1016/0301-9268(94)00070-8

Knauth, L. P., & Kennedy, M. J. (2009). The late Precambrian greening of the Earth. *Nature*, *460*(7256), 728–732. https://doi.org/10.1038/nature08213

Korte, C., & Kozur, H. W. (2010). Carbon-isotope stratigraphy across the Permian-Triassic boundary: A review. *Journal of Asian Earth Sciences*, *39*(4), 215–235. https://doi.org/10.1016/j.jseaes.2010.01.005

Lei, L. D., Shen, J., Li, C., Algeo, T. J., Chen, Z. Q., Feng, Q. L., et al. (2017). Controls on regional marine redox evolution during Permian-Triassic transition in South China. *Palaeogeography, Palaeoclimatology, Palaeoecology*, *486*, 17–32. https://doi.org/10.1016/j.palaeo.2017.02.010

Li, L. J., Liao, Z. W., Lei, L. D., Lash, G. G., Chen, A. Q., & Tan, X. F. (2020). On the negative carbon isotope excursion across the Wuchiapingian–Changhsingian transition: A regional event in the lower Yangtze region, South China? *Palaeogeography, Palaeoclimatology, Palaeoecology*, *540*, 109501. https://doi.org/10.1016/j.palaeo.2019.109501

Li, S., Wignall, P. B., Poulton, S. W., Hedhli, M., & Grasby, S. E. (2022). Carbonate shutdown, phosphogenesis and the variable style of marine anoxia in the late Famennian (Late Devonian) in western Laurentia. *Palaeogeography, Palaeoclimatology, Palaeoecology*, *589*, 110835. https://doi.org/10.1016/j.palaeo.2022.110835

Luo, G. M., Kump, L. R., Wang, Y. B., Tong, J. N., Arthur, M. A., Yang, H., et al. (2010). Isotopic evidence for an anomalously low oceanic sulfate concentration following end-Permian mass extinction. *Earth and Planetary Science Letters*, *300*(1–2), 101–111. https://doi.org/10.1016/j.epsl.2010.09.041

Luo, G. M., Wang, Y. B., Yang, H., Algeo, T. J., Kump, L. R., Huang, J. H., & Xie, S. C. (2011). Stepwise and large-magnitude negative shift in $\delta^{13}C_{carb}$ preceded the main marine mass extinction of the Permian–Triassic crisis interval. *Palaeogeography, Palaeoclimatology, Palaeoecology*, *299*(1–2), 70–82. https://doi.org/10.1016/j.palaeo.2010.10.035

Meyer, K. M., Kump, L. R., & Ridgwell, A. (2008). Biogeochemical controls on photic-zone euxinia during the end-Permian mass extinction. *Geology*, *36*(9), 747–750. https://doi.org/10.1130/g24618a.1

Müller, J., Sun, Y., Yang, F., Fantasia, A., & Joachimski, M. (2022). Phosphorus cycle and primary productivity changes in the Tethys Ocean during the Permian-Triassic transition: Starving marine ecosystems. *Frontiers in Earth Science*, *10*, 832308. https://doi.org/10.3389/feart.2022.832308

Müller, J., Sun, Y. D., Yang, F., Regelous, M., & Joachimski, M. M. (2023). Manganous water column in the Tethys Ocean during the Permian-Triassic transition. *Global and Planetary Change*, *222*, 104067. https://doi.org/10.1016/j.gloplacha.2023.104067

Musashi, M., Isozaki, Y., Koike, T., & Kreulen, R. (2001). Stable carbon isotope signature in mid-Panthalassa shallow-water carbonates across the Permo-Triassic boundary: Evidence for ^{13}C-depleted superocean. *Earth and Planetary Science Letters*, *191*(1–2), 9–20. https://doi.org/10.1016/s0012-821x(01)00398-3

Newby, S. M., Owens, J. D., Schoepfer, S. D., & Algeo, T. J. (2021). Transient ocean oxygenation at end-Permian mass extinction onset shown by thallium isotopes. *Nature Geoscience*, *14*(9), 678–683. https://doi.org/10.1038/s41561-021-00802-4

Nielsen, J. K., & Shen, Y. (2004). Evidence for sulfidic deep water during the Late Permian in the East Greenland Basin. *Geology*, *32*(12), 1037–1040. https://doi.org/10.1130/g20987.1

Payne, J. L., Lehrmann, D. J., Wei, J., Orchard, M. J., & Knoll, A. H. (2004). Large perturbations of the carbon cycle during recovery from the end-Permian extinction. *Science*, *305*(5683), 506–509. https://doi.org/10.1126/science.1097023

Poulton, S. W. (2021). *The iron speciation paleoredox proxy*. Cambridge University Press.

Poulton, S. W., & Canfield, D. E. (2005). Development of a sequential extraction procedure for iron: Implications for iron partitioning in continentally derived particulates. *Chemical Geology*, *214*(3–4), 209–221. https://doi.org/10.1016/j.chemgeo.2004.09.003

Poulton, S. W., & Canfield, D. E. (2011). Ferruginous conditions: A dominant feature of the ocean through Earth's history. *Elements*, *7*(2), 107–112. https://doi.org/10.2113/gselements.7.2.107

Reinhard, C. T., Planavsky, N. J., Gill, B. C., Ozaki, K., Robbins, L. J., Lyons, T. W., et al. (2017). Evolution of the global phosphorus cycle. *Nature*, *541*(7637), 386–389. https://doi.org/10.1038/nature20772

Scotese, C. R. (2014). Atlas of Middle and Late Permian and Triassic Paleogeographic Maps. Maps 43-48 from volume 3 of the paleomap atlas for ArcGIS (Jurassic and Triassic) and maps 49-52 from volume 4 of the paleomap PaleoAtlas for ArcGIS (Late Paleozoic). In *Mollweide Projection, PALEOMAP Project, Evanston, IL*.

Shen, S., Crowley, J. L., Wang, Y., Bowring, S. A., Erwin, D. H., Sadler, P. M., et al. (2011). Calibrating the end-permian mass extinction. *Science*, *334*(6061), 1367–1372. https://doi.org/10.1126/science.1213454

Shen, S. Z., Cao, C. Q., Zhang, H., Bowring, S. A., Henderson, C. M., Payne, J. L., et al. (2013). High-resolution $\delta^{13}C_{carb}$ chemostratigraphy from latest Guadalupian through earliest Triassic in South China and Iran. *Earth and Planetary Science Letters*, *375*, 156–165. https://doi.org/10.1016/j.epsl.2013.05.020

Stanley, S. M. (2016). Estimates of the magnitudes of major marine mass extinctions in earth history. *Proceedings of the National Academy of Sciences of the United States of America*, *113*(42), E6325–E6334. https://doi.org/10.1073/pnas.1613094113

Sun, Y. D. (2024). Dynamics of nutrient cycles in the Permian–Triassic oceans. *Earth-Science Reviews*, *258*, 104914. https://doi.org/10.1016/j.earscirev.2024.104914

Sun, Y. D., Joachimski, M. M., Wignall, P. B., Yan, C. B., Chen, Y. L., Jiang, H. S., et al. (2012). Lethally hot temperatures during the Early Triassic greenhouse. *Science*, *338*(6105), 366–370. https://doi.org/10.1126/science.1224126

Sweeney, R. E., & Kaplan, I. R. (1973). Pyrite framboid formation: Laboratory synthesis and marine sediments. *Economic Geology*, *68*(5), 618–634. https://doi.org/10.2113/gsecongeo.68.5.618

Twitchett, R. J., Krystyn, L., Baud, A., Wheeley, J. R., & Richoz, S. (2004). Rapid marine recovery after the end-Permian mass-extinction event in the absence of marine anoxia. *Geology*, *32*(9), 805–808. https://doi.org/10.1130/g20585.1

Wang, H., He, W. H., Xiao, Y. F., Yang, T. L., Zhang, K. X., Wu, H. T., et al. (2023). Stagewise collapse of biotic communities and its relations to oxygen depletion along the north margin of Nanpanjiang Basin during the Permian-Triassic transition. *Palaeogeography, Palaeoclimatology, Palaeoecology*, *621*, 13. https://doi.org/10.1016/j.palaeo.2023.111569

Wignall, P. B., & Hallam, A. (1992). Anoxia as a cause of the Permian/Triassic extinction: Facies evidence from northern Italy and the western United States. *Palaeogeography, Palaeoclimatology, Palaeoecology*, *93*(1–2), 21–46. https://doi.org/10.1016/0031-0182(92)90182-5

Wignall, P. B., Hallam, A., Lai, X. L., & Yang, F. Q. (1995). Palaeoenvironmental changes across the Permian/Triassic boundary at Shangsi (N. Sichuan, China). *Historical Biology*, *10*(2), 175–189. https://doi.org/10.1080/10292389509380519

Wignall, P. B., & Newton, R. (1998). Pyrite framboid diameter as a measure of oxygen deficiency in ancient mudrocks. *American Journal of Science*, *298*(7), 537–552. https://doi.org/10.2475/ajs.298.7.537

Wilkin, R. T., Arthur, M. A., & Dean, W. E. (1997). History of water-column anoxia in the Black Sea indicated by pyrite framboid size distributions. *Earth and Planetary Science Letters*, *148*(3–4), 517–525. https://doi.org/10.1016/s0012-821x(97)00053-8

Wilkin, R. T., Barnes, H. L., & Brantley, S. L. (1996). The size distribution of framboidal pyrite in modern sediments: An indicator of redox conditions. *Geochimica et Cosmochimica Acta*, *60*(20), 3897–3912. https://doi.org/10.1016/0016-7037(96)00209-8

Woods, A. D., Zonneveld, J.-P., & Wakefield, R. (2023). Hyperthermal-driven anoxia and reduced productivity in the aftermath of the Permian-Triassic mass extinction: A case study from Western Canada. *Frontiers in Earth Science*, *11*, 1323413. https://doi.org/10.3389/feart.2023.1323413

Wu, S. Q., Chen, Z. Q., Fang, Y. H., Pei, Y., Yang, H., & Ogg, J. (2017). A Permian-Triassic boundary microbialite deposit from the eastern Yangtze Platform (Jiangxi Province, South China): Geobiologic features, ecosystem composition and redox conditions. *Palaeogeography, Palaeoclimatology, Palaeoecology*, *486*, 58–73. https://doi.org/10.1016/j.palaeo.2017.05.015

Xiang, L., Schoepfer, S. D., Zhang, H., Yuan, D. X., Cao, C. Q., Zheng, Q. F., et al. (2016). Oceanic redox evolution across the end-Permian mass extinction at Shangsi, South China. *Palaeogeography, Palaeoclimatology, Palaeoecology*, *448*(SI), 59–71. https://doi.org/10.1016/j.palaeo.2015.10.046

Xiang, L., Zhang, H., Schoepfer, S. D., Cao, C. Q., Zheng, Q. F., Yuan, D. X., et al. (2020). Oceanic redox evolution around the end-Permian mass extinction at Meishan, South China. *Palaeogeography, Palaeoclimatology, Palaeoecology*, *544*, 109626. https://doi.org/10.1016/j.palaeo.2020.109626

Xiao, Y. F., Wu, K., Tian, L., Benton, M. J., Du, Y., Yang, H., & Tong, J. N. (2018). Framboidal pyrite evidence for persistent low oxygen levels in shallow marine facies of the Nanpanjiang Basin during the Permian-Triassic transition. *Palaeogeography, Palaeoclimatology, Palaeoecology*, *511*, 243–255. https://doi.org/10.1016/j.palaeo.2018.08.012

Xie, S. C., Pancost, R. D., Huang, J. H., Wignall, P. B., Yu, J. X., Tang, X. Y., et al. (2007). Changes in the global carbon cycle occurred as two episodes during the Permian-Triassic crisis. *Geology*, *35*(12), 1083–1086. https://doi.org/10.1130/g24224a.1

Yang, F., Li, S., An, K., Bond, D., Ao, R., Wu, X., et al. (2024). Supporting Information for: Re-evaluating Water Column Reoxygenation in the Aftermath of the End Permian Mass Extinction [Dataset]. *Zenodo*. https://doi.org/10.5281/zenodo.12776615

Yang, F., Sun, Y. D., Frings, P. J., Luo, L., E, J. W., Wang, L. N., et al. (2022). Collapse of Late Permian chert factories in the equatorial Tethys and the nature of the Early Triassic chert gap. *Earth and Planetary Science Letters*, *600*, 117861. https://doi.org/10.1016/j.epsl.2022.117861

Yang, H., Chen, Z. Q., Mei, X., & Sun, Y. D. (2021). Early Triassic microconchids from the Perth Basin, Western Australia: Palaeoecology and flourishing in the aftermath of the end-Permian mass extinction. *Geological Journal*, *56*(12), 6210–6222. https://doi.org/10.1002/gj.4115